RSC Advances

PAPER

View Article Online
View Journal | View Issue

Cite this: *RSC Adv.*, 2026, **16**, 8682

Ternary heteroatom (B, P, N) doped graphene for high-performance supercapacitors

Amanpreet Kaur, O. P. Pandey and Loveleen K. Brar *

Batteries and supercapacitors have become essential energy storage solutions, valued for their compact design, lightweight nature, and rapid energy delivery. However, traditional carbon-based supercapacitors are hindered by low energy density and limited charge storage capacity. To overcome these limitations, efforts have focused on tailoring carbon materials through heteroatom doping. In this work boron, phosphorous and nitrogen ternary codoped graphene (BPNG) samples were synthesized. FESEM, Raman and XPS analysis confirmed the morphology, structural integrity and bonding environment of the synthesized samples. The incorporation of 1.08 at%, 0.34 at% and 6.94 at% of B, P, and N, respectively for the optimized BPNG sample was confirmed by XPS analysis. This sample demonstrated outstanding properties with a specific capacitance of 450.86 F g^{-1}, significantly surpassing dual-doped (*e.g.*, B, N-doped: 129.93 F g^{-1} and B, P-doped: 155.65 F g^{-1}) and single-doped variants (B-doped: 152.5 F g^{-1}, P-doped: 211.6 F g^{-1}, N-doped: 98.25 F g^{-1}). The synergistic interaction among the three dopants significantly enhances the overall electrochemical performance: boron improves charge mobility, phosphorus contributes pseudocapacitive behavior, and nitrogen increases surface activity and wettability. A symmetric supercapacitor device, assembled using optimized BPNG delivered a high capacitance of 130.02 F g^{-1}, an energy density of 23.4 Wh kg^{-1}, and a power density of 692.31 W kg^{-1} under standard slow charge–discharge conditions. The device also retained over 84.62% capacitance after 5000 cycles, demonstrating excellent cycling stability. The stable cycling and high energy-power outputs reveal its promising potential to be used in next-generation energy-storage technologies.

Received 10th December 2025
Accepted 5th February 2026

DOI: 10.1039/d5ra09572g

rsc.li/rsc-advances

1 Introduction

With the escalating global energy demand, the development of clean, efficient, and sustainable energy storage technologies has become a critical priority for addressing future energy and environmental challenges. Modern society's growing reliance on renewable energy sources—such as wind and solar—has further driven the demand for more effective and reliable energy storage systems.[1] Supercapacitors have emerged as one of the most promising and stable energy storage devices, bridging the power and energy density gap between capacitors and batteries.[2–5] Their advantages include high power density, fast charge–discharge capability, long cycle life, and operational safety, making them ideal for various modern applications.[6,7] Today, supercapacitors are utilized across a wide range of sectors, including electric vehicles (*e.g.*, Tesla Model S), heavy-duty trucks, trains, and buses, as well as the emergency doors of the Airbus A380. They are also employed in microgrids to inject power during peak demand and in regenerative braking systems for plug-in hybrid electric vehicles.[6,8,9] Supercapacitors are generally classified into three main types based on their charge storage mechanisms and electrode materials: (i) electric double-layer capacitors (EDLCs), (ii) pseudocapacitors, and (iii) hybrid supercapacitors. The hybrid supercapacitors combine the reversible non-faradaic ion adsorption/desorption of EDLCs with the faradaic redox reactions occurring on the electrode surface of pseudocapacitors. In such systems, hybrid electrode materials—typically formed by integrating conductive carbon with transition-metal oxides—play a crucial role in enhancing overall performance. The carbon framework provides high conductivity, large surface area, and rapid ion pathways, while the metal oxide offers abundant redox-active sites for charge storage. When the carbon component is tuned through doping or defect engineering, its electronic structure and surface chemistry improve, enabling faster charge transfer and more efficient redox activity. These features collectively enhance energy storage with minimal loss in power density—ideal for applications such as wind turbines and energy recovery systems.[10–13]

Among the various carbon-based candidates, graphene has emerged as a particularly compelling choice owing to its exceptional electrical conductivity, high surface area, and structural stability. These attributes make graphene highly suitable for rapid and reversible ion adsorption, positioning it

Department of Physics and Material Science, Thapar Institute of Engineering and Technology, Patiala, Punjab 147004, India. E-mail: amanpreetk199595@gmail.com; oppandey@thapar.edu; brarloveleen@thapar.edu

as a strong foundation for the EDLC-type electrode in hybrid and asymmetric supercapacitor systems. However, the charge storage properties of pristine graphene are largely restricted due to limited density of electrochemically active sites, the tendency of sheets to restack due to strong van der Waals forces and its hydrophobic nature. These factors reduce accessible surface area and hinder ion transport.

To overcome these intrinsic limitations, heteroatom doping (B, N, P, S) has become a powerful strategy for tailoring graphene's characteristics.[14–16] This modification not only increases the specific surface area but also introduces additional pseudocapacitive sites, thereby improving overall charge storage capacity. Heteroatom doping in graphene also induces charge redistribution and defect formation, creating more electroactive sites and improving conductivity.[17,18] These features enhance charge transfer, electron mobility, and ion diffusion, making doped graphene highly effective for supercapacitor application. Doped graphene not only retains its original EDLC characteristics but also delivers supplementary pseudocapacitance, enabling a significantly enhanced charge-storage capability.

In asymmetric supercapacitors, where one electrode typically follows faradaic mechanism and the other the EDLC mechanism, such engineered graphene materials are particularly advantageous. Doped graphene effectively bridges the kinetic and capacitance gap between the carbon-based and faradaic electrodes, leading to faster ion/electron transport, reduced internal resistance, and a broader stable operating voltage window. These combined improvements translate into higher energy density, improved power output, and superior cycling durability—making doped graphene an ideal and versatile base material for next-generation high-performance energy-storage devices.

Ternary heteroatom doping has shown superior performance compared to dual and single-atom doping, owing to the synergistic effects and stronger interactions between electrolyte ions and the three distinct dopants. Ternary doping approach leads to improved electrical conductivity, better wettability, and more efficient ion transport, making it a promising route for next-generation energy storage devices.[19] Boron is a superior codopant in graphene frameworks. Boron as a p-type dopant with electron-deficient nature, complements the n-type behavior of other heteroatoms leading to a charge redistribution within the graphene matrix. The heteroatom-induced sites enhance the adsorption and redox activity of electroactive species, resulting in improved charge transfer kinetics and ion diffusion.

Ternary doping involving boron, nitrogen, and phosphorus (B, N, P) has primarily been limited to amorphous carbon frameworks.[20,21] To date, the simultaneous codoping of B, P, and N into the graphene lattice has not been systematically explored. In this study, we systematically investigate boron-centered ternary codoping strategies to tailor the structural and electrochemical properties of graphene. This rationally engineered B, P, N codoped graphene (BPNGn (n = 1–3)) exhibits remarkable supercapacitor performance. In this study, we present an optimized BPNG sample that incorporates all three dopants in a balanced manner. The synergistic interaction among the three heteroatoms results in enhanced defect density, improved electronic conductivity, and enriched surface functionality. These features collectively contribute to superior ion transport and charge storage, making the material highly suitable for advanced supercapacitor applications.

2 Materials and methods

2.1 Synthesis of codoped graphene

The synthesis of BPNGn (n = 1–3) samples were carried out using boric acid (H_3BO_3, 99.5–100%, Loba Chemie, India), potassium dihydrogen phosphate (KH_2PO_4, 98%, Loba Chemie, India) and urea (CH_4N_2O, 99%, Loba Chemie, India) as boron, phosphorus, and nitrogen precursors, respectively. The BPNG

Table 1 Details of synthesized samples

			XPS (at%)				
Sample name	Precursors/concentration	I_D/I_G	C	O	B	P	N
BG	H_3BO_3: 1.8 mM	1.088	81.85	15.37	2.72	—	—
PG	KH_2PO_4: 1.8 mM	1.090	86.47	13.28	—	0.26	—
NG	CH_4N_2O: 1.8 mM	1.073	82.04	8.59	—		9.38
BNG	H_3BO_3: 1.8 mM CH_4N_2O: 1.8 mM	1.217	81.50	9.10	3.75	—	5.60
BPG	H_3BO_3: 1.8 mM KH_2PO: 1.8 mM	1.140	74.60	19.70	3.96	1.20	—
BPNG1	H_3BO_3: 1.8 mM KH_2PO_4: 1.8 mM CH_4N_2O: 1.8 mM	1.120	86.27	10.48	0.15	0.02	3.06
BPNG2	H_3BO_3: 3.6 mM KH_2PO_4: 3.6 mM CH_4N_2O: 3.6 mM	1.220	82.03	9.52	1.08	0.34	6.94
BPNG3	H_3BO_3: 3.6 mM KH_2PO_4: 5.4 mM CH_4N_2O: 3.6 mM	1.140	71.55	18.55	5.45	2.08	0.59

Fig. 1 Schematic for synthesis of BPNG*n* samples followed by symmetric coin cell characterization.

samples were prepared by varying the concentrations of these precursors in the initial solution, following the same methodology reported in our previous work.[22] Briefly, the required amounts of boric acid, potassium dihydrogen phosphate, and urea as mentioned in Table 1, were ultrasonically mixed in 20 mL of synthesized GO dispersion (1.4 mg mL^{-1}). Synthesis of GO was discussed in Section S1 in SI. The mixture was then transferred to a Teflon-lined autoclave and subjected to hydrothermal treatment at 180 °C for 12 hours. The complete synthesis schematic is given in Fig. 1. For comparison, single and dual doped graphene samples (BG, PG, NG, BPG and BNG) were also synthesized using the same procedure. Table 1 gives the details of all the synthesized samples.

2.2 Characterizations

The structural and morphological features of the synthesized materials were investigated using a field emission scanning electron microscope (FESEM, Carl Zeiss Sigma 500) operating at an accelerating voltage of 15 kV. Surface chemistry and elemental composition were analyzed through X-ray Photoelectron Spectroscopy (XPS), conducted on a Thermo Scientific NEXA system equipped with a monochromatic Al Kα X-ray source (energy = 1486.6 eV). The powdered samples were mounted on a conductive platform using a high-purity silver base. Raman spectroscopy was utilized to identify structural disorders and defects, using a Horiba LabRAM system with a 532 nm argon ion laser.

2.3 Supercapacitance studies

The electrochemical performances of the synthesized samples were systematically evaluated using a Bio-Logic EC Lab SP300 workstation. A three-electrode configuration in 1 M H_2SO_4 was employed, with a glassy carbon electrode (GCE) as the working electrode, Pt wire as the counter electrode, and a saturated calomel electrode (SCE) as the reference. The electrochemical behavior was characterized using cyclic voltammetry (CV), galvanostatic charge–discharge (GCD), and electrochemical impedance spectroscopy (EIS). EIS spectra were obtained across the 50 mHz to 200 kHz frequency range, providing insights into the charge transfer kinetics and interfacial resistance of the electrodes. Among all samples, the one exhibiting the highest specific capacitance under these conditions was selected for further testing in 1 M H_2SO_4 utilizing graphite felt as a conductive current collector to simulate device-level performance. Also, a symmetric device was fabricated using graphite felt. Procedure for fabrication of working electrodes and device fabrication are mentioned in S2 of SI.

3. Results and discussion

Swetha

3.1 FESEM

Fig. S2 and 2 show SEM/FESEM images for all the synthesized samples. All single-doped samples exhibited wrinkled and distorted sheet-like structures, arising from structural perturbations created by heteroatom incorporation (Fig. S2(a–c)). In boron and nitrogen doped samples (BG, NG), the basal plane remained largely preserved as atomic sizes of B and N were close to that of carbon, resulting in moderate wrinkling due to slight lattice distortion. In contrast, PG showed more pronounced deformation and sheet warping because the larger phosphorus atom disrupts the graphene lattice more strongly, inducing partial rehybridization from sp^2 toward sp^3 and increasing the degree of crumpling.[7,22–24] These trends become more prominent in dual and ternary doped structures. In BNG sample, the graphene sheets appeared wrinkled and partially opened, while BPG samples displayed more distorted and disordered morphologies due to the stronger lattice mismatch and structural strain introduced by phosphorus. When B, N, and P were simultaneously incorporated, as in the BPNG*n* series, their combined effect creates a strongly disordered, expanded, and more open graphene network. Nitrogen promoted sheet opening and defect formation, phosphorus induced asymmetry and curvature, and boron enhanced lattice distortion while tuning the electronic environment. Among the ternary doped samples, BPNG2 (Fig. 2) exhibited the most evident degree of wrinkling, opening, and sheet distortion compared to BPNG1 and BPNG3, suggesting an optimal balance of dopant incorporation. BPNG2 sample seemed to have an expanded and increased accessible surface area which might ultimately enhance charge storage and boost supercapacitor performance.

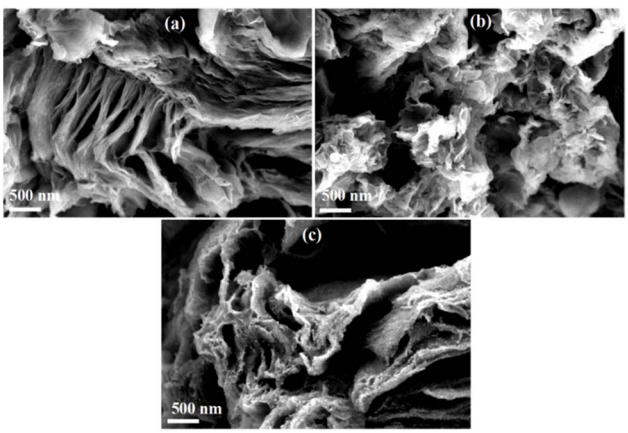

Fig. 2 FESEM images (a) BPNG1, (b) BPNG2, and (c) BPNG3 samples.

3.2 XPS

XPS analysis was carried out to investigate the surface chemistry and elemental composition of the synthesized samples. Survey spectra of single (BG, NG, and PG), dual (BNG and BPG) (Fig. S3(a)) and ternary (BPNG*n* (n = 1–3)) doped samples (Fig. 3(a)) and the corresponding elemental data (Table 1) confirmed the successful incorporation of heteroatoms. Signals in survey spectra corresponding to boron (B), phosphorus (P) and nitrogen (N) were clearly detected in all the samples, verifying their presence within the graphene framework. The incorporation of B, P, and N increased in the BPNG2 sample due to the doubled precursor amount. When P precursor amount was further increased in BPNG3 sample, it enhances B and P uptakes and decreases N incorporation. This indicates that the incorporation of larger P atoms, beginning at the sheet edges, expanded and opened the layered structure, thereby facilitating the subsequent uptake of B atoms and restricts n-type N atoms.

The deconvoluted high-resolution XPS spectra and fitting parameters for BG, NG, PG, BNG and BPG samples are displayed in Fig. S3(b–h) and Table S1. Deconvoluted C 1s and O 1s spectra with fitted parameters of BPNG*n* (n = 1–3) samples are shown in Fig. S4 and Table S2. The B 1s peak fitting posed a challenge due to its overlap with the P 2s signal; however, this region was successfully resolved into six components—five corresponding to B 1s and one to P 2s (Fig. 3(b), Fig. S3(g)) in BPNG*n* (n = 1–3) and BPG samples, respectively. To accurately quantify boron content, the area under the P 2s peak was subtracted and is reflected in the values listed in Table 2. The B 1s peaks for BPNG*n* (n = 1–3) samples were assigned to B–C/B–P, BC_2O, B–N, BCO_2 and B_2O_3 bonding environments, indicating

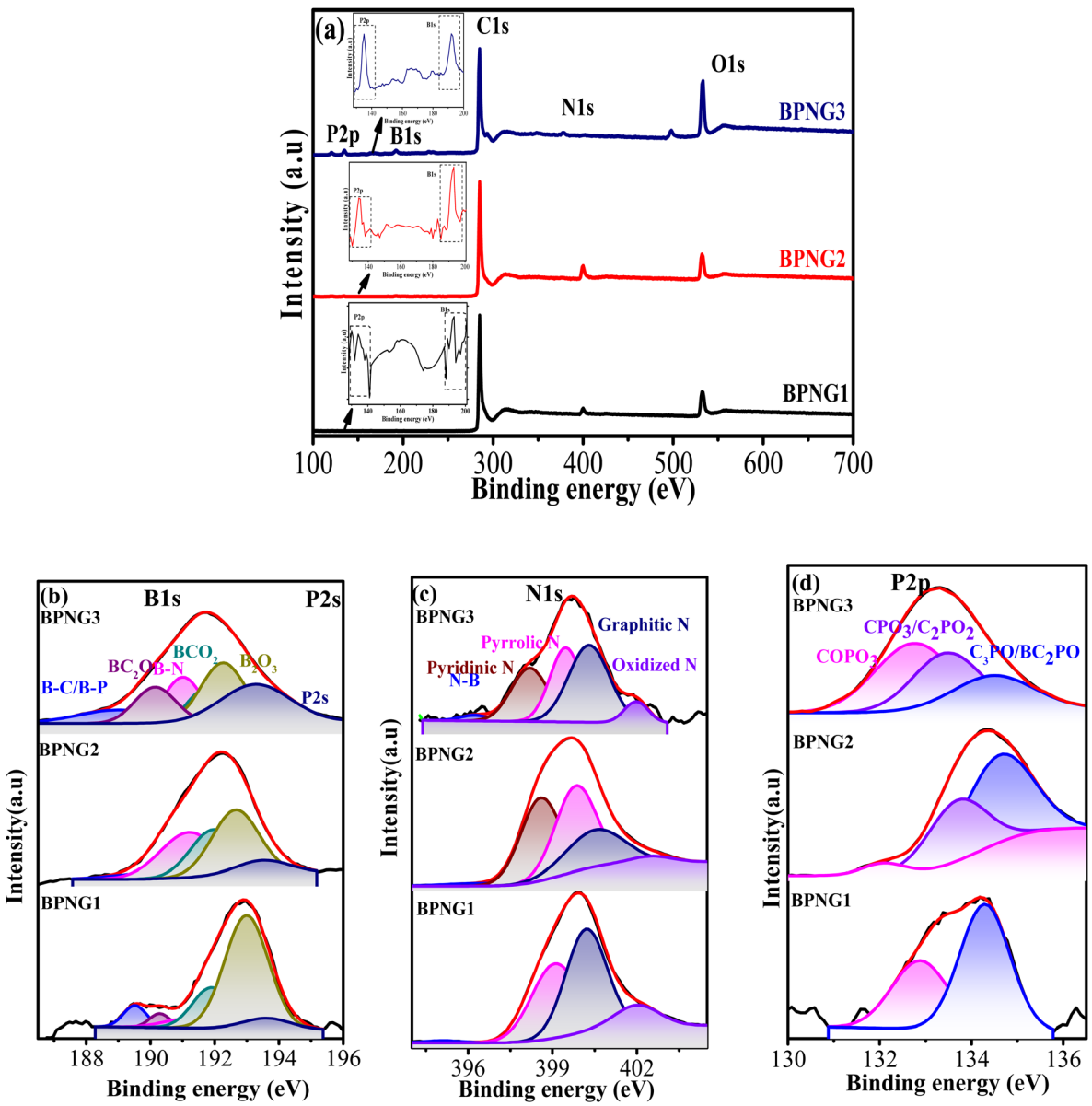

Fig. 3 (a) XPS Survey spectra, high resolution spectra of (b) B 1s, (c) N 1s, and (d) P 2p for BPNG*n* (n = 1–3) samples.

Table 2 XPS parameters obtained from deconvoluted high resolution spectra of B 1s, P 2p, and N 1s for synthesized BPNG*n* (n = 1–3) samples

	Moieties	BPNG1	BPNG2	BPNG3
B 1s	B–C/B–P	6.09	3.88	10.53
	BC_2O	3.48	4.70	14.16
	B–N	5.78	28.09	16.01
	BCO_2	52.51	23.19	9.55
	B_2O_3	25.97	33.08	25.06
P 2p	$COPO_3$	34.39	4.72	44.92
	CPO_3/C_2PO_2/P–N	9.27	35.44	32.87
	C_3PO/BC_2PO	56.33	59.88	22.21
N 1s	N–B	0.90	2.00	1.96
	Pyridinic N	5.11	35.04	24.22
	Pyrrolic N	37.77	37.23	28.90
	Graphitic N	46.04	23.02	38.64
	Oxidized N	10.17	2.69	6.20

successful integration of boron in both oxygenated and covalent frameworks within the graphene matrix. Atomic percentages of these moieties are shown in Table 2. For the P 2p peak, deconvolution revealed three main configurations: C_3PO/BC_2PO, C_2PO_2/CPO_3/P–N, and $COPO_3$ (Fig. 3(c)). Among these, the C_3–P═O structure, a trigonal pyramidal configuration, was known for its thermodynamic stability and minimal formation energy.[25,26]

The high-resolution N 1s spectra was deconvoluted into five distinct components, corresponding to different nitrogen bonding configurations within the graphene lattice (Fig. 3(d)). These included N–B, pyridinic N, pyrrolic N, graphitic N, and oxidized N species. The presence of N–B confirms successful interaction between nitrogen and boron atoms, while pyridinic and pyrrolic nitrogen species are typically associated with edge defects.[27–29]

The optimized BPNG2 sample has high content of B–N, B_2O_3, CPO_3/C_2PO_2, pyridinic and pyrrolic N moieties. In BPNG3 sample, higher P content, enhances thermodynamically less stable $COPO_3$ moieties, which distorts the local carbon framework and occupy substitutional sites there by suppressing nitrogen incorporation. In contrast, BPNG1 and BPNG2 samples contains relatively low P content, allowing P to predominantly stabilize in the energetically favorable C_3PO moieties. These moieties were mainly located at graphene edge sites and their lowest formation energy supports spontaneous and stable embedding of P. The high presence of graphitic C_3PO structure enhances lattice stability and leaves more substitutional carbon sites accessible for nitrogen, resulting in higher N incorporation in BPNG1 and BPNG2 compared to BPNG3.

3.3 XRD

The XRD patterns of synthesized single, dual doped (Fig. S5(a)), and BPNG (n = 1–3) samples (Fig. 4(a)) show the characteristic graphene reflections at ~26° (002) and ~42° (10), confirming partial graphitization and the formation of few-layer graphene. In the BPNG2 and BPNG3 samples, additional weak peaks at ~17°, 30°, 34°, and 45°—absent in BPNG1—are assigned to

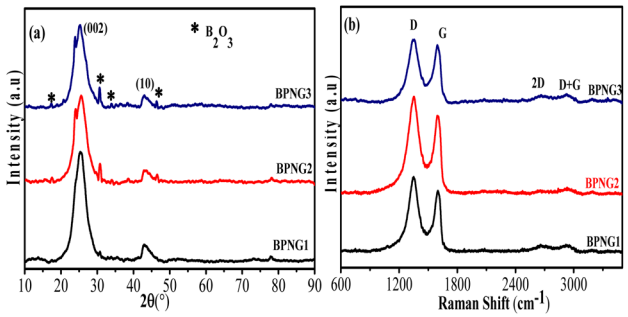

Fig. 4 (a) XRD and (b) Raman plot for BPNG*n* (n = 1–3) samples.

crystalline B_2O_3. The low intensity of these reflections relative to the dominant (002) peak indicates that only a small portion of the total boron forms B_2O_3,[30] whereas the majority is incorporated into the graphene lattice, contributing to the broadening and shoulder development near the (002) region. When the boron content exceeds the substitutional limit of the carbon framework under simultaneous B, N, and P codoping, the excess boron does not integrate into the lattice but instead oxidizes and segregates as surface or edge-attached B_2O_3 domains, giving rise to the observed additional peaks.

3.4 RAMAN

The Raman spectra of the synthesized single (BG, NG, and PG), dual (BNG and BPG) and ternary (BPNG*n* (n = 1–3)) samples in Fig. S5(b) and Fig. 4, respectively showed distinct features characteristic of graphene-based materials. Two prominent peaks appeared near 1350 cm^{-1} and 1590 cm^{-1} corresponding to the D and G bands, respectively. The D band was attributed to structural defects, edge disorder, and sp^3-hybridized carbon introduced by heteroatom doping, while the G band originated from the in-plane vibrations of sp^2-hybridized carbon atoms, indicating graphitic structure. A 2D band was observed around 2693 cm^{-1}, resulting from a second-order two-phonon resonance process and providing insight into the number of graphene layers. In addition, a weaker band near 2926 cm^{-1}, corresponding to the (D + G) combination mode, further reflected the presence of disorder and defect-related vibrational features in the carbon lattice.[3,31] A comparison of the intensity ratio I_D/I_G revealed a higher value for BPNG2 than BPNG1 and BPNG3, indicating a greater degree of disorder and defect density in BPNG2 as compared to other samples. BPNG2 contained a high content of N present predominantly as pyridinic and pyrrolic nitrogen, thus introducing more numerous defect sites as compared to BPNG1 and BPNG3 samples as corroborated by XPS analysis.

3.5 Electrochemical property

The electrochemical properties of BPNG*n* (n = 1–3) electrodes were studied using Electrochemical Impedance Spectroscopy (EIS) in 0.1 M KCl containing 5.0 mM $[Fe(CN)_6]^{3-/4-}$ to probe charge-transfer behaviour at the electrode–electrolyte interface. Fig. S6 shows the Nyquist plots for BNG and BPG, while Fig. 5

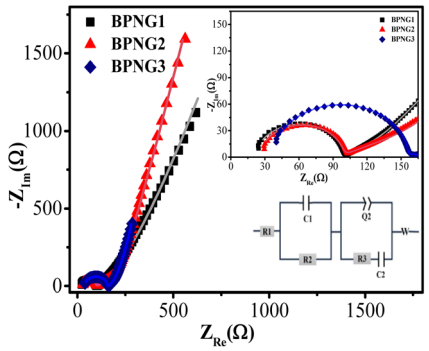

Fig. 5 EIS responses for BPNG*n* (n = 1–3) samples in 0.1 M KCl electrolytic solution containing 5 mM of $Fe(CN)_6^{3-/4}$ (Inset: Fitted circuit and EIS response curves at high frequencies).

displays those for BPNG*n* (n = 1–3), with the inset highlighting the high-frequency region. The inset of Fig. 5 presents the fitted equivalent circuit, where R_1, R_2, and R_3 denote the electrode resistance, electrolyte resistance, and combined charge- and mass-transfer resistances, respectively, while C_1 represents interfacial capacitance and Q_2/C_2 describe pseudocapacitive and double-layer contributions.

Among the dual-doped samples, BPG showed better performance than BNG due to its lower R_2 and R_3 enabling faster ion and electron transport. In the ternary-doped series, BPNG2 outperformed both BPNG1 and BPNG3, as well as the binary samples, owing to its optimal combination of low R_2 and R_3 for smooth charge transfer and a strong pseudocapacitive component that enhanced redox activity. BPNG1 exhibited higher R_3 and a very low Q_2, whereas BPNG3 showed high R_2 and weak pseudocapacitance (Table 3), which limited their overall electrochemical behavior. These results highlighted that ternary doping in BPNG2 provided the most effective balance between conductivity and redox performance.

3.6 Supercapacitance

To evaluate the capacitive performance of the electrode materials, CV and GCD tests were performed using a standard three-electrode setup. Fig. 6(a) illustrates the CV responses for comparative performance of the BPNG*n* (n = 1–3), dual doped BPG and BNG samples to realize impact of doping, recorded at a scan rate of 10 mV s^{-1} in 1 M H_2SO_4. All samples exhibited a quasi-rectangular CV shape, characteristic of dominant EDLC behavior. Notably, the presence of subtle redox peaks within the loops reveals additional pseudocapacitive contributions,

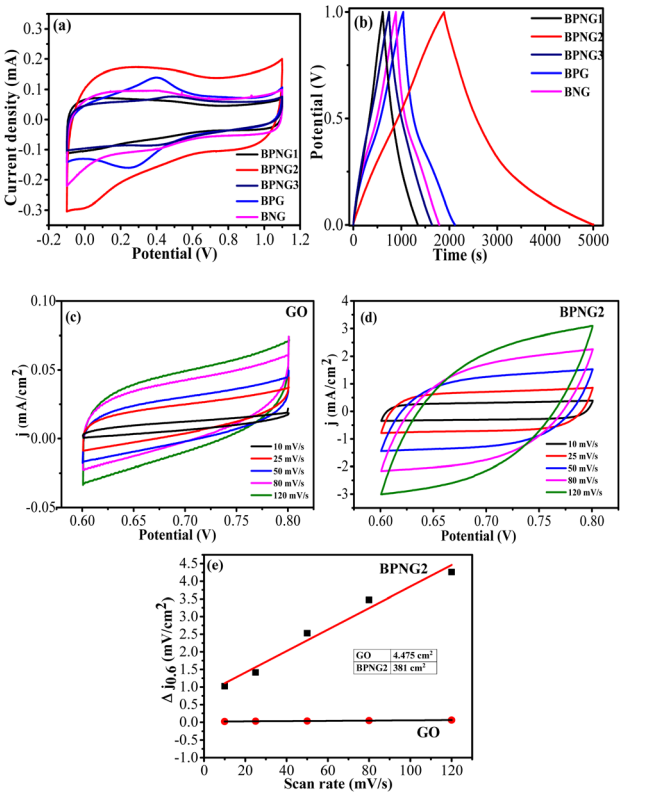

Fig. 6 (a) CV curves at 10 mV s^{-1} scan rate, (b) GCD curves at 0.145 A g^{-1} for BPNG*n* (n = 1–3) and BPG and BNG samples. ECSA plots, CV at different scan rates for (c) synthesized GO, (d) BPNG2, and (e) plot of scan rates *vs.* current densities ($\Delta J_{0.6}$) for GO and BPNG2 samples.

originating from reversible faradaic reactions at electroactive sites introduced by B, P, and N co-doping. These redox features confirmed the presence of functional groups capable of enhancing charge storage. Among all, BPNG2 sample showed the largest CV area curve, indicating superior electrochemical performance and the highest specific capacitance (Table 4).

Fig. 6(b) presents the GCD curves of the synthesized BPNG*n* (n = 1–3) samples. All samples displayed nearly symmetric triangular profiles, highlighting the dominance of EDLC behavior. Among them, the BPNG2 sample exhibited the broadest charge–discharge curve, reflecting its enhanced charge storage capacity. Table 4 confirms the superior performance of the BPNG2 electrode. The possible reason for enhanced supercapacitance was attributed to synergistic effect of optimized content of three codopants and their enhanced contents, which

Table 3 EIS parameters for BPNG*n* (n = 1–3) samples in 0.1 M KCl electrolytic solution containing 5 mM of $Fe(CN)_6^{3-/4}$

Sample	R_1 (Ω)	C_1 (F)	R_2 (Ω)	Q_2 (F $s^{(a-1)}$)	a_2	R_3 (Ω)	C_2 (F)	s ((Ω)^2)
BNG	32.63	8.30×10^{-10}	137.20	1.06×10^{-4}	0.75	25.21	3.90×10^{-3}	300.50
BPG	8.78	9.32×10^{-10}	95.11	9.12×10^{-5}	0.62	27.06	1.34×10^{-3}	226.00
BPNG1	23.06	1.26×10^{-9}	76.21	8.23×10^{-5}	0.46	80.17	2.32×10^{-3}	386
BPNG2	23.77	1.21×10^{-9}	73.53	0.93×10^{-3}	0.45	70.69	0.74×10^{-3}	222.8
BPNG3	28.12	0.79×10^{-9}	118.50	0.14×10^{-3}	0.38	16.22	5.44×10^{-3}	93.94

Table 4 Specific capacitance of synthesized GO, single (BG, NG and PG), dual (BNG and BPG) and ternary (BPNG*n* (n = 1–3)) doped graphene samples

Sample	CV (3 mV s^{-1})	CP (0.145 A g^{-1})
GO	4.66	3.70
BG	122.95	152.51
NG	88.34	98.25
PG	155.27	184.90
BNG	122.43	129.93
BPG	133.89	155.65
BPNG1	88.27	107.34
BPNG2	258.91	450.86
BPNG3	98.39	129.34

was supported by XPS, Raman results. Also, BPNG2 exhibits high content of CPO_3/C_2PO_2/P–N, C_3PO/BC_2PO, BC_2O, B–N, B_2O_3, Pyridinic N and Pyrrolic N moieties. Role of moieties are as follow:

(i). CPO_3, C_2PO_2, and C_3PO were tetrahedral phosphorus-oxygen functional groups that were crucial for charge redistribution and enhanced electrochemical stability in doped graphene. The C_3–P═O configuration was notably stable and plays a key role in stabilizing the electrochemical interface between the electrode and electrolyte and also enhances wettability. P–N created more n-type sites that enhances charge transfer.[32]

(ii). Combined boron and phosphorus doping, forming structures like BC_2PO, further modulated electronic properties by creating a p–n co-doping effect, facilitated efficient ion adsorption and rapid charge transfer, ultimately enhancing the rate capability and overall capacitance of graphene-based supercapacitor electrodes.

(iii) The formation of B–N bonds led to localized surface polarization, generating highly reversible redox-active sites that boosted and stabilized pseudocapacitive behavior. Additionally, the elevated presence of BC_2O species contributed further to faradaic charge storage. The oxidation of boron at edge sites results in the formation of BCO groups, which improved electrolyte wettability and facilitate better ion access, thereby enhancing specific capacitance.[22]

(iv). B_2O_3 moieties situated at the edges of doped graphene, significantly enhanced the surface area and acted as dominant active sites, effectively facilitating selective electron transfer kinetics.[33]

(v). Pyridinic N played a key role in facilitating charge transfer by introducing edge-located active sites, while pyrrolic N enhanced electrolyte interaction and ion diffusion through improved surface polarity.[34]

The enhanced supercapacitive performance of the BPNG2 electrode arises from the synergistic interaction of boron, phosphorus, and nitrogen dopants. The overall B, N, and P contents in ternary doped (BPNG2) sample are lower than those in dual-doped (BNG, BPG) samples, but shows enhanced supercapacitance in comparison to dual doped samples. We attribute this enhancement to synergy between the three dopants. There is enhancement in the pseudocapacitive moieties in the ternary system, including B_2O_3, pyrolic N as well as phosphorus–oxygen species (CPO_3/C_2PO_2 and C_3PO/BC_2PO) which introduces abundant defects and modifies the local electronic structure, creating additional active sites and facilitate rapid surface redox reactions for charge storage. The cooperative interaction among all these bonding motifs enhances electron delocalization, charge polarization, and electrolyte accessibility, resulting in superior utilization of active sites and higher specific capacitance in ternary doped graphene (BPNG2) than dual-doped samples.

The large difference between CV and GCD value (Table 4) arises because of enhanced content of phosphorus with nitrogen dopants which introduces slow, diffusion-controlled redox sites that were not fully accessed during the fast potential sweep in CV. These sites became active over the longer timescale of GCD, leading to a much higher GCD value and a wider gap between the results from two techniques.[35–37] Table 5 shows the comparable high specific capacitance value as reported in literature.

To further examine the electrochemical activity of the synthesized samples, the electrochemically active surface area (ECSA) was determined by evaluating the electrochemical double-layer capacitance (C_{dl}) obtained from cyclic voltammetry (CV) measurements conducted in a non-faradaic potential window (0.6–0.8 V). It directly reflects the real, electrolyte-accessible surface under operating electrochemical conditions. Unlike N_2 adsorption, which is performed at cryogenic temperature and probes gas-accessible pores that may remain electrochemically inactive, ECSA—derived from double-layer capacitance—captures the actual active sites involved in ion adsorption, charge transfer, and redox processes in the electrolyte. For heteroatom-rich graphene systems, where surface polarity, defect density, and electrolyte interaction dominate performance, ECSA provides a more realistic and performance-relevant assessment of surface availability. Fig. 6(c and d) shows the CV curves of GO and BPNG2 recorded at different scan rates,

Table 5 The Specific capacitance values obtained from the literature and the present work on heteroatoms-incorporated graphene

Material	Specific capacitance	Current density	Electrolyte	References
B/S-rGO	345 F g^{-1}	1 A g^{-1}	1 M H_2SO_4	38
PB-rGO	436 F g^{-1}	1 A g^{-1}	1 M H_2SO_4	39
BNUG	325.5 F g^{-1}	1 A g^{-1}	1 M H_2SO_4	31
CFNG	363 F g^{-1}	0.5 A g^{-1}	1 M H_2SO_4	40
BPNG2	450.86 F g^{-1}	0.15 A g^{-1}	1 M H_2SO_4	Present work

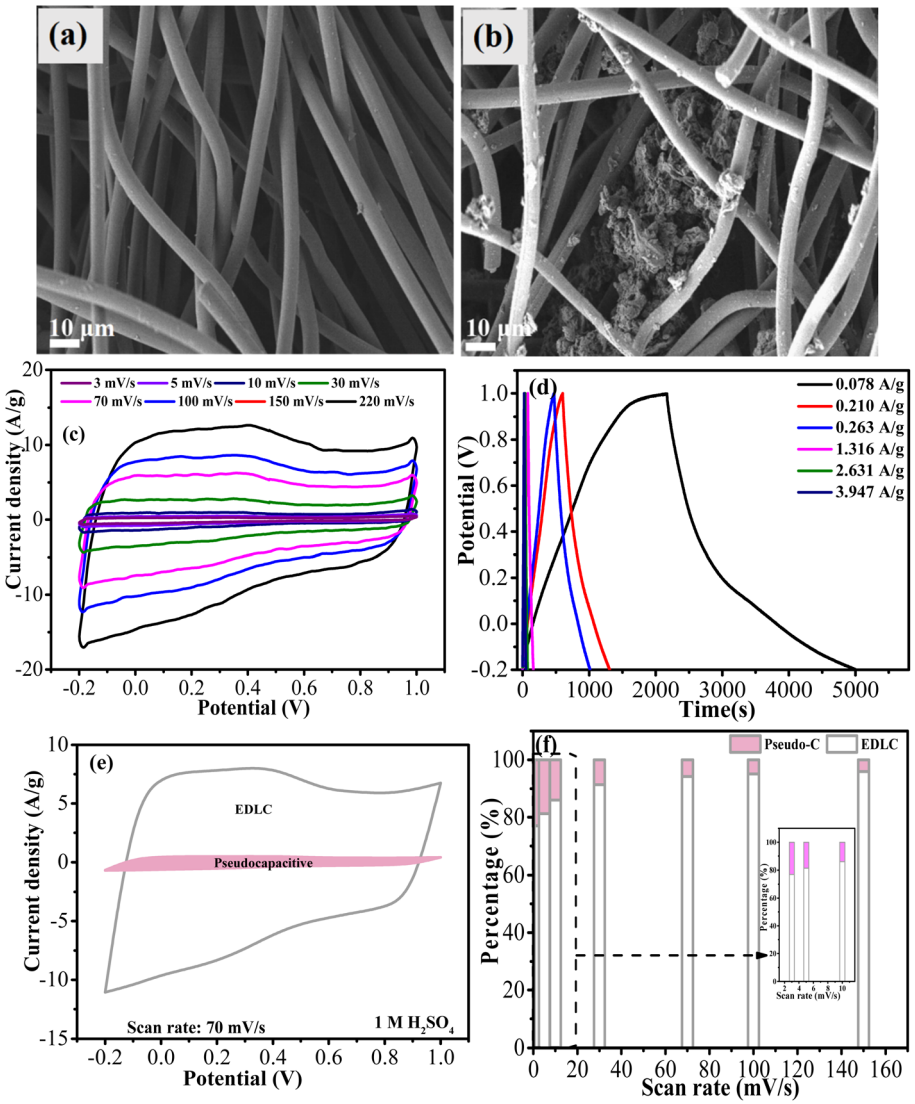

Fig. 7 FESEM images (a) bare graphite felt and (b) BPNG2 modified graphite felt electrode at different magnifications. (c) CV curves at different scan rates, (d) GCD curves at different current densities (e) capacitance contribution plot at 70 mV s^{-1} scan rate, and (f) capacitance contribution ratios of Pseudocapacitance (Pseudo-C) and EDLC for BPNG2 modified graphite felt electrode.

where the capacitive current increases proportionally with scan rate, confirming dominant double-layer charging behavior. Fig. 6(e) presents the linear relationship between the current density difference ($\Delta J_{0.6}$) and scan rate, from which the C_{dl} values were extracted. The ECSA values were calculated using the relation ECSA = C_{dl}/C_S, where C_S is the specific capacitance of a smooth carbon surface (0.040 mF cm^{-2}). Pristine GO exhibits a very low ECSA of 4.475 cm^2, indicating limited electrochemically accessible surface area due to sheet restacking and poor electrolyte penetration. In contrast, BPNG2 displays a markedly enhanced ECSA of 381 cm^2, reflecting the presence of abundant electrochemically active sites. This enhanced ECSA is consistent with the pronounced improvement in specific capacitance, which increases dramatically from 3.70 F g^{-1} for GO to 450.86 F g^{-1} for BPNG2, demonstrating much more effective charge accumulation at the electrode–electrolyte interface. The large rise in capacitance originates from dopant-induced surface activation, improved wettability, and efficient utilization of electrochemically accessible sites.[41,42] The simultaneous enhancement in ECSA and specific capacitance clearly confirms the effectiveness of ternary B, P, and N co-doping in promoting superior electrochemical performance.

Fig. 7(a and b) presents FESEM images of bare graphite felt and BPNG2-modified graphite felt. Both samples exhibit a characteristic fibrous network structure. The pristine graphite felt displayed a porous framework with numerous voids, which provide a favorable surface for anchoring the BPNG2 material, thereby facilitated rapid electron transport and efficient charge transfer. In comparison, the modified felt clearly showed deposition of the BPNG2 sample along the fibre surfaces. The BPNG2 sample was further evaluated for its electrochemical performance using a graphite felt current collector. Fig. 7(c) displays CV curves at different scan rates in 1 M H_2SO_4, where the quasi-rectangular shape confirms predominant EDLC

behavior. Redox humps in CV curves indicated redox process between oxygen atoms and protons of acidic electrolyte. Fig. 7(d) shows the corresponding GCD curves at different current densities, also recorded in 1 M H_2SO_4. BPNG2 modified graphite felt electrode showed specific capacitance of 186.4 F g^{-1} at 0.072 A g^{-1}. It evidently determined that discharge period is inversely proportional to applied current density.

To further evaluate the effect of heteroatom doping on the capacitive performance of BPNG2 on graphite felt, Dunn's method was employed to quantify the relative contributions of electric double-layer capacitance (EDLC) and pseudo-capacitance (pseudo-C)(Fig. 7(e)). The Dunn's method differentiates between rate-independent (surface-controlled, EDLC) and diffusion-controlled (pseudo-C) processes based on current response. In this approach, the current (i) is modeled using the equation $i = K_1v + K_2v^{0.5}$, where K_1v represents the EDLC component and $K_2v^{0.5}$ accounts for the pseudo-C contribution. The analysis revealed that BPNG2 exhibited the high EDLC contribution at all the scan rates (Fig. 7(f)). Fig. 7(f) clearly reveals that EDLC contribution increases with scan rate.

A symmetric supercapacitor device was fabricated utilizing 1.0 M H_2SO_4 in a two electrode system to evaluate the performance of BPNG2 electrode in practical applications. Fig. 8(a) shows reaction mechanism in BPNG2//BPNG2 symmetric cell. CV curves at different scan rates displays EDLC (quasi-rectangular shape) and faradaic behaviour (redox peak)(Fig. 8(b)). At high scan rate diffusion limitation of electrolyte ions on electrode material could lead to deviate from rectangular shape. BPNG2//BPNG2 shows specific capacitance of 130.02 F g^{-1} at 0.32 A g^{-1} current density. Fig. 8(c) displays quasi-triangular shape with little IR drop at different current densities demonstrates low resistance and electrochemical reversibility.

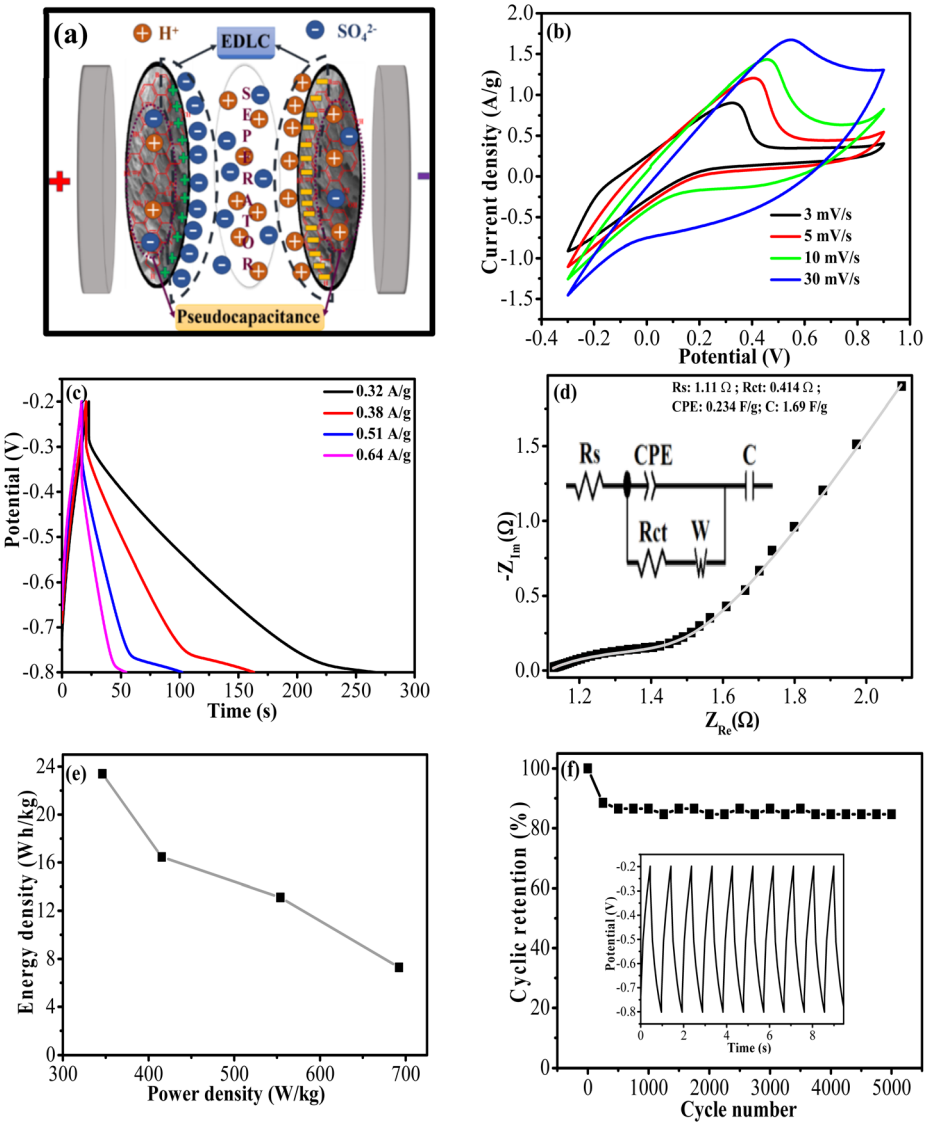

Fig. 8 (a) BPNG2//BPNG2 symmetric cell mechanism. (b)CV curves at different scan rates, (c) GCD curves at different current densities, (d) EIS plot, (e) Ragone plot, and (f) cycling stability; inset: first 10 GCD curves for BPNG2//BPNG2 symmetric supercapacitor device.

Table 6 Comparison of carbon-based and doped-graphene symmetric supercapacitor devices

Device	Electrolyte	Specific cap. (F g^{-1})	Energy density (Wh kg^{-1})	Power density (W kg^{-1})	Ref.
Symmetric: N-doped 3D graphene	1 M $EMIMBF_4$	62	54	1224	43
Symmetric: N, S co-doped carbon	1 M H_2SO_4	88.45	33.85	562.5	44
Symmetric: Porous carbon nanosheet	1 M Na_2SO_4	>45	~12.2	>3349	45
Symmetric: N, S co-doped bamboo carbon	1 M H_2SO_4	—	21.2	454	46
Symmetric: BPNG2	1 M H_2SO_4	130.02	23.4	692.31	Present work

Fig. 8(d) presents the EIS plots for the BPNG2//BPNG2 symmetric device. EIS analysis was conducted to investigate the ion diffusion behavior and charge transport kinetics within the cell. The corresponding fitted equivalent circuit model used to interpret the impedance data. R_s and R_{ct} in equivalent circuit were attributed to the solution resistance and charge transfer resistances, respectively. CPE (constant phase element; 0.234 F g^{-1}) and C (1.69 F g^{-1}) signifies pseudocapacitance and double-layer capacitance, respectively. It displays lowest 1.11 Ω and 0.414 Ω R_s and R_{ct} values, corroborated with smallest arc in lower frequency region. Fig. 8(e) represents ragone plot for BPNG2//BPNG2 symmetric device. The maximum energy density was 23.4 Wh kg^{-1} with power density of 346.15 W kg^{-1} at 0.32 A g^{-1} current density. The maximum power density of 692.31 W kg^{-1} is comparable and better than carbon based symmetric devices. For durability test, charge–discharge curves (3.85 A g^{-1}) were performed (Fig. 8(f)). First 10 charge discharge curves are shown in inset of Fig. 8(f). Declining up to 250 cycle, capacitance retention starts stabilizing and attains good value of 84.62% after 5000 cycles.

Table 6 compares the electrochemical performance of recently reported carbon-based and doped-graphene symmetric supercapacitor devices. In comparison, the BPNG2 symmetric device (present work) exhibits the highest specific capacitance (130.02 F g^{-1}) among the listed materials, reflecting efficient ion diffusion and enhanced redox activity from B, P, N doping. Its balanced energy and power density further confirm that multi-element doping significantly improves charge storage capability.

4 Conclusion

The optimized ternary doped graphene sample, synthesized with boron (1.08 at%), phosphorus (0.34 at%), and nitrogen (6.94 at%), exhibited remarkable electrochemical performance, highlighting the effectiveness of triple heteroatom doping. The electrode achieved a high specific capacitance of 450.86 F g^{-1}, outperforming dual-doped samples like B, N-doped (129.93 F g^{-1}) and B, P-doped (155.65 F g^{-1}), as well as single-doped variants such as B-doped (152.5 F g^{-1}), P-doped (211.6 F g^{-1}), and N-doped (98.25 F g^{-1}). This enhancement is attributed to the combined effects of boron improving charge mobility, phosphorus inducing pseudocapacitive behavior, and nitrogen enhancing surface activity and wettability. The symmetric device based on optimized BPNG*n* delivered a capacitance of 130 F g^{-1}, an energy density of 23.4 Wh kg^{-1}, and a power density of 692.31 W kg^{-1}, while maintaining over 84.62% capacitance retention after 5000 cycles, confirming its excellent stability and practical potential in energy storage applications.

Author contributions

Amanpreet Kaur: methodology, formal analysis, validation, investigation and writing – original draft. O. P. Pandey: supervision, writing – review and editing. Loveleen Kaur Brar: conceptualization, supervision, visualization, writing – review and editing.

Conflicts of interest

There are no conflicts to declare.

Data availability

The data supporting the findings of this study are available from the corresponding author upon request. All the data generated or analysed during this study are included in this article and its supplementary information (SI). Supplementary information is available. See DOI: https://doi.org/10.1039/d5ra09572g.

Acknowledgements

The authors want to acknowledge DST FIST-2 Sponsored Materials Characterization Facility for FESEM and Raman spectroscopy and IIT Mandi for XPS characterizations. Authors are also thankful to TIET for funding.

References

1 M. Khandelwal, C. Van Tran, J. Lee and J. Bin In, *Chem. Eng. J.*, 2021, **428**, 131119.
2 Y. Wang, Z. Chang, M. Qian, T. Lin and F. Huang, *Chem. Eng. J.*, 2019, **375**, 122054.
3 X. Zou, D. Wu, Y. Mu, L. Xing, W. Zhang, Z. Gao, F. Xu and K. Jiang, *Carbon*, 2019, **159**, 94–101.
4 Z. Chen, L. Hou, Y. Cao, Y. Tang and Y. Li, *Appl. Surf. Sci.*, 2018, **435**, 937–944.
5 M. Pal, A. Pal, P. Pal and M. Nandi, *ACS Appl. Eng. Mater.*, 2023, **1**, 2965–2983.

6 R. M. Dell, P. T. Moseley and D. A. J. Rand, *Batteries and Supercapacitors for Use in Road Vehicles*, 2014.
7 R. Kumar, S. Sahoo, E. Joanni, R. K. Singh, K. Maegawa, W. K. Tan, G. Kawamura, K. K. Kar and A. Matsuda, *Mater. Today*, 2020, **39**, 47–65.
8 E. Pipitone and G. Vitale, *J. Power Sources*, 2020, **448**, 227368.
9 Q. Zhang, L. Wang, G. Li and Y. Liu, *J. Energy Storage*, 2020, **31**, 101721.
10 S. Suresh Balaji, D. Sangamithirai, K. R. Gopi Krishna and A. Pandurangan, *Energy and Fuels*, 2024, **38**, 15721–15743.
11 Z. Zhu, Y. Men, W. Zhang, W. Yang, F. Wang and Y. Zhang, *eScience*, 2024, **4**, 100249.
12 X. Zhao, X. Wang, P. Gao, P. Zhao, J. Wang and Y. Li, *Green Energy Environ.*, 2025, **10**, 1256–1269.
13 Y. Zheng, J. Yang, Z. Liu and Z. Qiao, *Adv. Mater.*, 2025, **37**, 10911.
14 G. Li, Y. Li, J. Deng, H. Lin, X. Hou and L. Jia, *Mater. Chem. Front.*, 2020, **4**, 2704–2715.
15 S. S. Balaji, M. Karnan, J. Kamarsamam and M. Sathish, *ChemElectroChem*, 2019, **6**, 1492–1499.
16 J. Li, X. Li, D. Xiong, L. Wang and D. Li, *Appl. Surf. Sci.*, 2019, **475**, 285–293.
17 K. Li, P. Li, Z. Sun, J. Shi, M. Huang, J. Chen, S. Liu, Z. Shi and H. Wang, *Green Energy Environ.*, 2023, **8**, 1091–1101.
18 L. Song, X. Zhong, F. Wang, Z. Huang and Z. Hong, *Rare Met.*, 2024, **43**, 4286–4301.
19 J. Liu, Y. Zhu, X. Chen and W. Yi, *J. Alloys Compd.*, 2020, **815**, 152328.
20 Y. Chang, H. Shi, X. Yan, G. Zhang and L. Chen, *Carbon*, 2020, **170**, 127–136.
21 N. Ahmad, N. Muhammad, H. Chen, J. Wang, C. Wei, M. Khan and R. Yang, *J. Colloid Interface Sci.*, 2023, **650**, 1725–1735.
22 A. Kaur, O. P. Pandey and L. K. Brar, *J. Phys. Chem. Solids*, 2023, **180**, 111460.
23 Y. Cao, W. Si, Y. Zhang, Q. Hao, W. Lei, X. Xia, J. Li and F. Wang, *FlatChem*, 2018, **9**, 1–7.
24 Y. Li, M. Chen, B. Liu, Y. Zhang, X. Liang and X. Xia, *Adv. Energy Mater.*, 2020, 1–36.
25 J. Meng, Z. Tong, H. Sun, Y. Liu, S. Zeng, J. Xu, Q. Xia, Q. Pan, S. Dou and H. Yu, *Adv. Sci.*, 2022, **9**, 1–10.
26 G. Moreno-Fernández, J. L. Gómez-Urbano, M. Enterría, R. Cid, J. M. López del Amo, R. Mysyk and D. Carriazo, *Electrochim. Acta*, 2020, **361**, 136985.
27 R. Li, C. Qin, X. Zhang, Z. Lin, S. Lv and X. Jiang, *RSC Adv.*, 2019, **9**, 1679–1689.
28 D. Guo, B. Ding, X. Hu, Y. Wang, F. Han and X. Wu, *ACS Sustain. Chem. Eng.*, 2018, **6**, 11441–11449.
29 Z. Sun, Z. Yan, K. Yue, A. Li and L. Qian, *Compos. Part B*, 2020, **196**, 108132.
30 Y. Gao, W. Rafaniello, M. F. Toksoy, T. Munhollon and R. Haber, *RSC Adv.*, 2015, 19067–19073.
31 P. M. Pandian and A. Pandurangan, *New J. Chem.*, 2021, **45**, 12408–12425.
32 Z. Bi, L. Huo, Q. Kong, F. Li, J. Chen, A. Ahmad, X. Wei, L. Xie and C. M. Chen, *ACS Appl. Mater. Interfaces*, 2019, **11**, 11421–11430.
33 M. Sookhakian, H. Ullah, M. A. Mat Teridi, G. B. Tong, W. J. Basirun and Y. Alias, *Sustain. Energy Fuels*, 2020, **4**, 737–749.
34 E. S. L. Niladri Talukder, Y. Wang and B. B. Nunna, *Carbon*, 2021, 198–214.
35 A. Pal, S. Ghosh, D. Singha and M. Nandi, *ACS Appl. Energy Mater.*, 2021, **4**, 10810–10825.
36 P. Nakhanivej, X. Yu, S. K. Park, S. Kim, J. Y. Hong, H. J. Kim, W. Lee, J. Y. Hwang, J. E. Yang, C. Wolverton, J. Kong, M. Chhowalla and H. S. Park, *Nat. Mater.*, 2019, **18**, 156–162.
37 A. Lia, Z. Guob, Q. Sunc, X. Daia, Y. Lic, S. Yia, K. Yaoc, X. Liud, Z. Baoe, J. Raoa and Y. Zhang, *The Lancent Pschch*, 2022, 1–35.
38 S. Sekar, P. Arumugam and G. Rajamanickam, *Fullerenes Nanotube Carbon Nanostructures*, 2023, 31, 845–855.
39 S. Surya, A. Pandurangan and R. Govindaraj, *J. Energy Storage*, 2024, **86**, 111319.
40 D. Johnsirani and A. Pandurangan, *Diam. Relat. Mater.*, 2020, **105**, 107800.
41 C. Wei, S. Sun, D. Mandler and X. Wang, *Chem. Soc. Rev.*, 2019, **48**, 2518–2534.
42 H. Ren, Y. Pan, C. C. Sorrell and H. Du, *J. Mater. Chem. A*, 2020, **8**, 3154–3159.
43 K. M. Joseph and V. Shanov, *Batteries*, 2022, **8**, 258.
44 A. A. Oladipo, *Mater. Chem. Phys.*, 2021, **260**, 124129.
45 Z. Li, B. Yang, K. Zou, L. Kong, M. Yue and H. Duan, *Carbon*, 2019, **144**, 540–548.
46 L. Ji, B. Wang, Y. Yu, N. Wang and J. Zhao, *Electrochim. Acta*, 2020, **331**, 135348.